Indian J Phys
https://doi.org/10.1007/s12648-024-03157-9

ORIGINAL PAPER

Opportunity of ferrimagnetic (CZLF)/ferroelectric (BZT) composite materials in high frequency applications

A M Altarawneh[1]*, A M A Henaish[1,2], R Ghazy[1], R M Shalaby[3], N A Abdelhakim[3], O M Hemeda[1] and M Mostafa[1]

[1]Physics Department, Faculty of Science, Tanta University, Tanta 31527, Egypt

[2]NANOTECH Center, Ural Federal University, Ekaterinburg 620002, Russia

[3]Metal Physics Laboratory Research, Department of Physics, Faculty of Science, Mansoura University, Mansoura 35516, Egypt

Received: 07 September 2023 / Accepted: 29 February 2024

Abstract: The ferrimagnetic $Zn_{0.35}Co_{0.65}$ $La_{0.02}Fe_{1.98}O_4$ (CZLF) ferrite with cubic spinel structure (space group Fd3*m*) was made into composite by mixing with ferroelectric $Ba_{0.5}Zr_{0.5}TiO_3$ (BZT) perovskite with tetragonal structure (space group P4*mm*) at the mass ratio. Disk-shaped composite powder was finally heated at 1100 °C to study the structure, dielectric and ferroelectric properties. The structural characterization for synthesized samples were carried out using Fourier transform infrared and Transmission Electron Microscopy. Fourier transform infrared show the successful formation of composite samples which is also observed from x-ray diffraction pattern. In compared to their ferrite counterparts before the composite, dielectric response and ferroelectric characteristics of the composite samples are noticeably altered. Compared to the ferrite samples, the composite system exhibits a higher permittivity. In composite samples, the space charge polarization, which was primarily effective at low frequencies and high measurement temperatures, is much diminished. The mechanical properties and indentation creep of these bearing alloys were studied by Vickers indentation testing at room temperature. The remnant polarization of BZT/CZLF increases with decreasing BZT content, which may be suitable for permanent memory device applications.

Graphical abstract

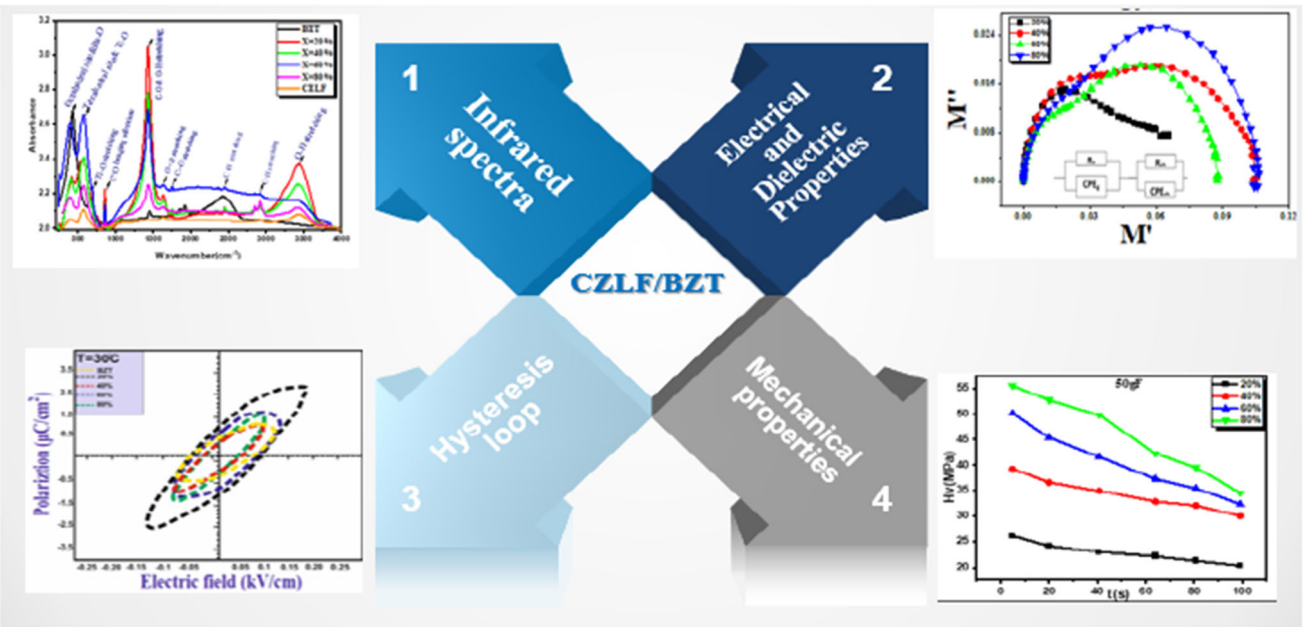

*Corresponding author, E-mail: aseelt682@gmail.com

Published online: 19 March 2024

Keywords: BZT-CZLF; Electric permittivity (ε); P–E hysteresis loop; Microhardness; Micro indentation creep

1. Introduction

Due to its extraordinary magnetostriction characteristic, spinel cobalt ferrite ($CoZnLaFe_2O_4$) is a material that has received much study and is potentially useful in the magnetic devices, electrochemical science and the field of electronics [1]. Cobalt zinc lanthanum ferrite is an ideal material for electronic and magnetic devices because of its noteworthy electrical capabilities and physically and chemically stable structure [2–4].

Significant research has recently been done to improve the electrical and structural characteristics of CZLF-based devices. Partially replacing Fe^{3+} ions, ferroelectric/piezoelectric composite materials and nanoparticles have received a lot of attention. Due to their exceptional ME coupling, CFO-based composites that combine the ferroelectric phase with ferromagnetic CZLF stand out among these heterostructure systems. It is interesting to note that magnetoelectricity may be detected in bulk and nanocomposite systems for CZLF and barium zirconium titanate ($BaZrTiO_3$) [5]. Perovskite $BaZrTiO_3$ is reported to cause structural alteration and lattice disorder in spinel CZLF, which may affect the electrical behavior and impedance characteristics in CZLF-BZT composites [6]. In order to distinguish the impedance of the grain from the impedances of other sources, such as the grain boundary and electrode interface, complex impedance spectroscopy is a highly elegant approach. The distribution of relaxation processes throughout a frequency range is revealed by this measurement. We have described the structural, ferroelectric, ferromagnetic and improved magnetoelectric properties of CZLF-BZT composites in our previous literature [7–9].

In this paper, we provide the results of a thorough analysis employing impedance spectroscopy of the electrical behavior and conductivity phenomena. The experimental technique, microstructural characterization and electrical characteristics of CZLF-BZT composites are discussed in the sections that follow. This research will be helpful in studying the usage of CZLF-BZT composites in high frequency applications with appropriate tuning for device development. It will also contribute to our understanding of electrical behavior [10–14].

2. Experimental details

2.1. Sample preparation

Composite samples $(1 - x)$ $BaZr_{0.5}Ti_{0.5}O_3$ (BZT) + (x) $Zn_{0.35}CO_{0.65}La_{0.02}Fe_{1.98}O_4$ (CZLF), (x = 20%, 40%, 60% and 80%, wt%) were prepared using high-energy ball milling technique. The ferroelectric phase (BZT) prepared by tartrate procedure method [15] and the ferrimagnetic phase (CZLF) prepared by flash auto combustion method [16], and the details about the process of high-energy ball milling could be found in a previous paper [17]. The powder was collected; then pellets were pressed at 5000 kg/cm^2 using the compressor with thickness d = 0.36 cm.

2.2. Physical measurements

The samples were examined by x-ray diffraction using a Philips model (PW-1729) diffractometer (Cu–Kα radiation source with λ = 1.540598 Å) with 2Θ in the range from 4° to 80° and the software was used for the refinements by Rietveld's profile analysis method. The prepared samples' Fourier transform infrared (FTIR) spectra were obtained at room temperature (RT) using a PerkinElmer 1430 instrument in the wavenumber range from 200 to 4000 cm^{-1}.The samples morphology was investigated using TEM (JEOL, Model: JEM-2100). The frequency-dependent electrical and dielectric properties of the Co–Zn–La spinel ferrites tablets were recorded by a high-precision LCR meter bridge (HP-6284A). The standard technique used for measuring the hardness of metals is the Vickers hardness test. Vickers hardness is a measure of the hardness of a material, calculated from the size of an impression produced under load by a pyramid-shaped diamond indenter.

3. Results and discussion

3.1. FTIR analysis

The FTIR analysis for $(1 - x)$ $BaZr_{0.5}Ti_{0.5}O_3$ (BZT) + (x) $Zn_{0.35}CO_{0.65}La_{0.02}Fe_{1.98}O_4$ (CZLF) composites, where x = (0, 20, 40, 60, 80 and 100%) were carried

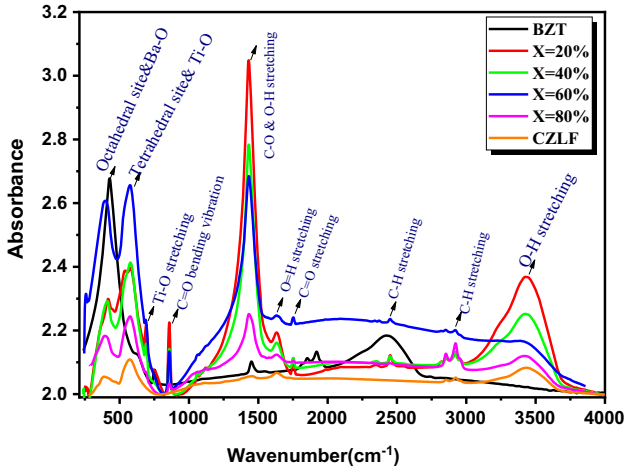

Fig. 1 FTIR of spectra of composite samples $(1 - x)$ $BaZr_{0.5}Ti_{0.5}O_3$ (BZT) + $xCo_{0.65}$ $Zn_{0.35}$ $La_{0.02}$ $Fe_{1.98}O_4$ (CZLF), where x = (0, 20, 40, 60, 80 and 100%)

out to investigate and give information about the phase identification for the studied composites. Figure 1 shows the FTIR spectra recorded at room temperature in wavelength range (200–4000 nm) of all BZT + CZLF composites which synthesizes using ball milling high-energy methods. The spectra show a typical IR absorption band of two main absorption bands assigned by v_1 and v_2, respectively. The position of v_1 is around 565 cm^{-1}, whereas the other band v_2 appears around 430cm^{-1}. An overlap occurs between the tetrahedral absorption bands of ferrite phase Fe^{+3}–O^{2-} "A" bond and that of ferroelectric phase arises from the stretching vibration of Ti–O bond. Another overlap occurs between octahedral absorption band of ferrite phase Fe^{+3}–O^{2-} "B" and the bending vibration of ferroelectric phase due to Ti–O bond [18]. This clearly show the successful formation of composite samples which is also observed from XRD pattern. The absorption bands are shifted toward higher frequency by increasing the ferrite phase content as given in Table 1. The effect of ferrite phase in the intermolecular structure can be explained by the shortening of the Ti–O bond and Fe^{+3}–O^{2-} bond leading to the increase in the vibration frequency and the force constant as given in Table 1. The small band appear at 800–1000 cm^{-1}, which its intensity decreases by increasing ferrite content may be due to carbon–oxygen bond vibration which arises from the use of tartaric acid in the preparation of ferroelectric phase. The shape and the width of absorption band depend on the cation distribution at both tetrahedral and octahedral sites. The intensity of absorption bands v_1 and v_2 for tetrahedral and octahedral sites, respectively, decreases by increasing ferrite phase content. This may be due to the decrease in BZT phase at both sites. For composite samples with double phases the bands appeared between 1457 cm^{-1}.

3.2. Transmission electron microscopy (TEM)

The TEM micrograph of $(1 - x)$ $BaZr_{0.5}Ti_{0.5}O_3$ (BZT) + (x) $Zn_{0.35}CO_{0.65}La_{0.02}Fe_{1.98}O_4$ (CZLF) where x = 20%, 40%, 60% and 80% for the as prepared samples are shown in Fig. 2a, which includes the electron diffraction patterns for these samples. It is clearly seen from the figure the presence of two types of particles the dark one reversed to the ferrite particle whereas the bright one reversed to ferroelectric phase (Table 2).

The concentration of ferrite particle increases by increasing the composite samples, at sample x = 80% the predominant particle type belongs to ferrite phase, beside the color of particles we can distinguishable between the two types by its particle size, we mean that the particle size of ferroelectric material, which may be due to the agglomeration caused magnetic particle [19].

The interface area between the particle size of two types are characterized by the present of dislocation to reduce the lattice strain energy. The crystallite size for cause ferroelectric and ferrimagnetic phases where deduced for TEM micrograph are in given Table 3 with the result calculated from x-ray pattern.

It was noted that particle size for ferro electric phase obtained from x-ray has values near that obtain TEM micrograph. The behavior of particle size for ferroelectric and ferrimagnetic phases has decreasing trend and

Table 1 The wavenumber (υ), The Force constant (F) of composite sample $(1 - x)$ $BaZr_{0.5}Ti_{0.5}O_3$ (BZT) + x $Co_{0.65}$ $Zn_{0.35}La_{0.02}Fe_{1.98}O_4$ (CZLF), where x = (0, 20, 40, 60, 80 and 100%)

x%	$v2$ cm^{-1}	$v1$ cm^{-1}	$F2$ (dyne/cm) × 10^4	$F1$ (dyne/cm) × 10^5
0	336	541	8.03	2.07
20	418	578	12.42	2.38
40	411	578	12.52	2.40
60	396	575	12.61	2.42
80	394	576	12.70	2.44
100	388	573	11.05	2.41

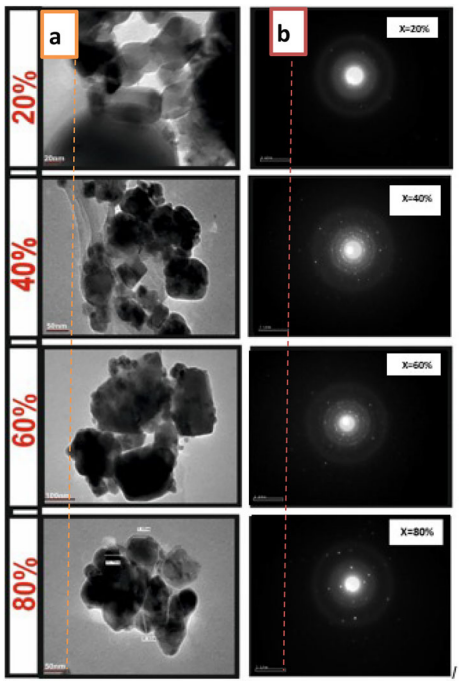

Fig. 2 (**a**) TEM images, and (**b**) selected area electron diffraction pattern for composite samples

increasing trend, respectively, by increasing the ferrite content [20]. The selected area of electron diffraction pattern is shown in Fig. 2b for all samples. The indexing of the rings indicates the presence of (311) ring which belongs to ferrite phase (outer ring) beside the ring (110) which belongs to ferroelectric phase (inner ring). The presents on to mean peak the two types phases indicates the successful preparation of our composite, without any chemical interaction between two phases. The appearance of regular rings in the electron diffraction pattern confirms the high crystallite of our samples.

3.3. Electrical and dielectric properties

3.3.1. Dielectric properties

The variation of permittivity ε' and ε'' for all ME composite $(1-x)$ $BaZr_{0.5}Ti_{0.5}O_3$ (BZT) $+ x$ $Co_{0.65}$ $Zn_{0.35}La_{0.02}Fe_{1.98}O_4$ (CZLF) are shown in Fig. 3. The dielectric constant values decreased with increasing frequency and by increasing the ferrite content up to $x = 60\%$ and then increase again for sample 80% ferrite content. However, the dielectric constant has high values at low frequency and low values high frequency. Which can be explained by the space charge polarization which is effective at low frequency and the ME composite obese the model of Maxwell–Wagner model of interfacial polarization [21]. The high value of dielectric constant (4×10^3–$2 \times 10^{4)}$ was due to the presence of ferroelectric material enclosed by ferrimagnetic. At high frequency the dielectric constant is nearly independent of frequency and the other type of polarization ionic, electronic and dipole polarization are negligible. The change in dielectric polarization with respect two frequency above 10^2 Hz was because of the incapability of the electric dipole to follow the external field frequency, at low frequency the large value high dielectric constant the charge polarization of ME composite. At high frequency the dipole rotation can't follow the variation external electric field frequency. The imaginary part ε' of p dielectric constant also decreases with the increase in frequency and decreases by the increase in the nano magnetic particle at low frequency [22].

Table 3 Relaxation times, grain size and radius of composite samples for CZLF with different x% content

x (%)	$\tau_{M''}(s)$	f max	Grain size (μm)	Radius (a.u)
20	1.07×10^{-5}	1.47×10^4	0.082	0.005
40	1.59×10^{-5}	1×10^4	0.097	0.012
60	1.06×10^{-5}	1.49×10^4	0.120	0.008
80	0.63×10^{-5}	2.48×10^4	0.175	0.020

3.3.2. Electric modulus spectra

Figure 4 shows the real and imaginary part of electric modulus (M' and M'') as a function of frequency and ferrite content. The electric modulus is used to study the dielectric relaxation process without discussing the effect of interface polarization. The complex dielectric (M^*) is defined as the inverse of the complex dielectric (ε^*). The real electric modulus M′ at low frequency region has a very low value near zero, which indicates the absence of interfacial

Table 2 The crystallite size (D) determined from TEM and x-ray for composite samples

x (%)	$D_{ferrite}$ from XRD (nm)	$D_{ferrite}$ from TEM (nm)	D_{ferro} from XRD (nm)	D_{ferro} from TEM (nm)
20	35.40	31	32.43	31.93
40	42.84	31.19	30.15	28.11
60	39.52	35.24	28.67	24.22
80	36.52	48.82	29.36	23.33

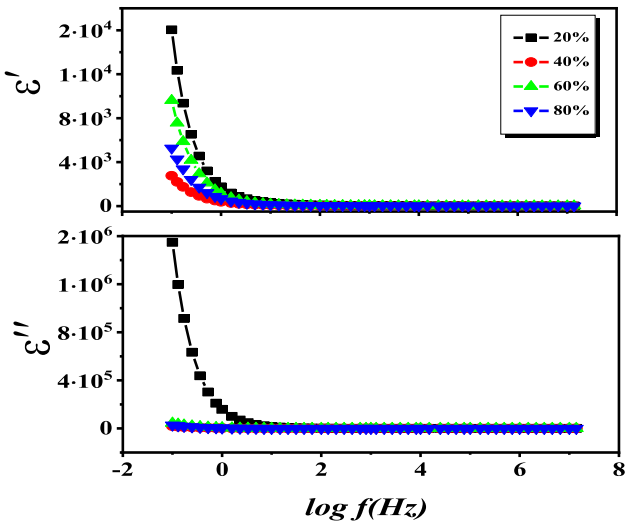

Fig. 3 Frequency dependence of ε' and ε'' of composite samples

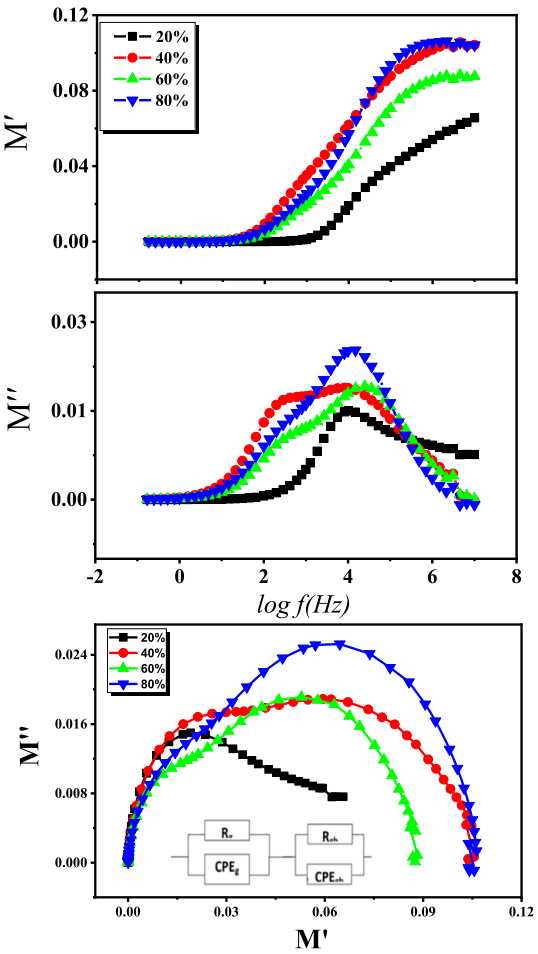

Fig. 4 Frequency dependence of the electric modulus spectra of composite samples

polarization effect. Then M' increases by increasing frequency and the increasing of nanomagnetic material content. The M'' has different behavior with the frequency variation and has a peak at certain frequency, which is shifted to higher frequency with increasing the concentration of ferrite content. The frequency at maximum value with its relaxation time $\tau_m = 1/2\pi f_{max}$ is given in Table 1.

By incorporating the ferrite phases the grain size increase from (TEM analysis) and the number of dipoles increase causing the decrease in relaxation time, this explain a good correlation the structure properties of the grain and relaxation process.

The cole–cole diagram for the nano composite sample. Its notice that each sample has its own semicircle with specified diameter. The bulk of semicircle represents at low frequency the resistance of grain boundary, whereas at high frequency it represents the resistance bulk grain. It was noticed that the diameters of semicircle increase by increasing ferrite content which is due to the increase in polarization and dielectric permittivity by increase ferrite content.

The cole–cole plots show a two-relaxation type explained by the presence of multi-semicircles varying upon the presence of the double relaxation effects associated with grain and grain boundary. The first one characterizes the resistance of the grain boundary related to low frequency, and the second characterizes the resistance of grain related to high frequency [23, 24]. This behavior is attributed to representing the sample by an electrical circuit as a combination of resistors and capacitors, through a configuration of two parallel RC equivalent circuits in series, which are used to represent the electrical response of ferrite. The values of Koop parameters of the grain, R_g, C_g, and the grain boundaries, R_{gb}, C_{gb}, are approximately applying the equations [21, 29]

$$M''_{\max} = \frac{\epsilon_o}{2C} \tag{1}$$

$$2\pi f_{\max} RC = 1 \tag{2}$$

And tabulated in Table 2. The capacitance and the resistance of grain is greater than the capacitance of grain. The values of Koop parameters are representing the whole dielectric behavior of the CZLF (Table 4).

3.3.3. *The dependence of the dielectric constant with temperature*

Figure 5 shows the variation of dielectric constant with temperature for composite sample at different ferrite content (x = 20%, 40%, 60% and 80%) fixed frequencies 10 kHz, 50 kHz and 100 kHz. It was noticed that the dielectric constant for sample x = 60% has the highest value among the other samples at fixed frequency 10 kHz, whereas the sample 80% has the highest value of dielectric constant at other frequency 50 kHz, 100 kHz. The ferrite phase affect strongly the dielectric properties of the

Table 4 Relaxation times and Koop parameters of grain and grain boundaries of composite samples for CZLF with different *x*% content

x (%)	$\tau_{M1''}$ (ns)	Cg (nf)	Rg (kΩ)	$\tau_{M2''}$ (μs)	Cgb (nf)	Rgb (kΩ)
20	19.4	0.29	55	0.159	0.29	1392
40	15.9	0.22	90	0.74	0.26	2725
60	10.6	0.23	24	0.01	0.40	1316
80	6.39	0.17	70	0.02	0.35	1647

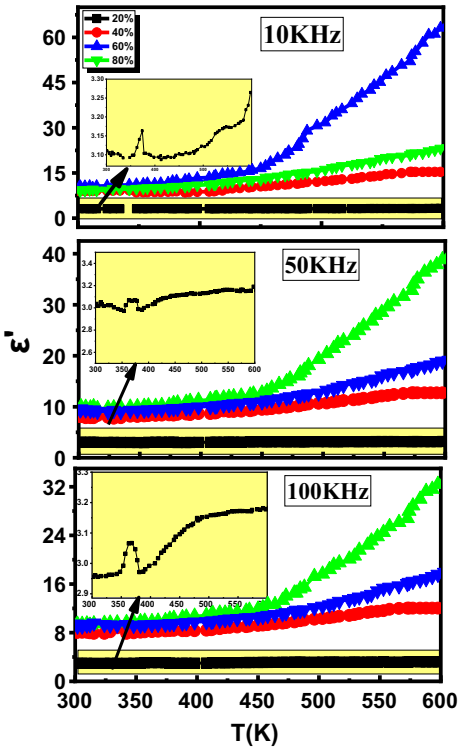

Fig. 5 Dielectric constant (ε) of composite samples

composite material, which contribute on rising the electronic polarization which deduced from the hopping electrons between $Fe^{+3} \leftrightarrow Fe^{+2}$. At low temperature the dielectric constant is nearly independent on room temperature and increases above certain temperature, were the mobility of electron becomes thermally activated which leads increase polarization and dielectric constant [25, 26]. From Table 5 it is noticed that value of Curie temperature for the ferrite sample is different from the T_c composite of the sample which mean that we can control the value of T_c just by adding the suitable ferrite content to the ferroelectric phase. The values of T_c for identical samples is not affected by the frequency change, whereas the values of dielectric constant decrease by increaseing frequency.

The transition temperature for ferroelectric phase is still appeared at sample $x = 20\%$ and disappeared for another sample, where the ferrite content become highest. The sample $x = 60\%$ and 80% have the lowest resistivity and highest values of conductivity consequently have the highest dielectric constant. This means that the mechanism of conduction is similar to mechanism of dielectric constant behavior.

3.3.4. *Ac conductivity*

Figure 6 shows the variation of *AC* resistivity for all composite samples for different frequency 10 kHz, 50 kHz and 100 kHz as a function of reciprocal temperature (1000/T). It is noticed from Fig. 6 that presence of three regions with two break points. Each region has its own conduction mechanism. The first (I) belong to the ferroelectric phase (BZT) were the (II) region belongs to ferrimagnetic phase (CZLF) and the last region belongs to paramagnetic phase. At region (II) the predominant conduction mechanism is the hopping electron between $Fe^{+3} \leftrightarrow Fe^{+2}$at octahedral site [27]. The first order transition between the region (II and III) is associated with the changed slope of the lines at certain point (Curie Temperature) of ferrimagnetic state and can be determined from Fig. 6 which are listed Table 6. In the first region (I) the predominant conduction mechanism belongs to ferro electric phase with a peak appear at the T_c. The figure shows the transformation point from ferroelectric to ferrimagnetic phase and listed in Table 6. This means that the relation between Ac resistivity and 1000/T can explain clearly the different conduction mechanism in the composite sample. The first (I) break point of ferroelectric phase include the structure phase transition from tetragonal to cubic phase. The first break point which is corresponding of T_c to ferroelectric phase shifts to lower temperature by increasing ferrite content which indicates the influence of ferrite content on the ferro electric phase. The second break point is due to the transition to ferrimagnetic to paramagnetic phase a high shifted to higher temperature by increasing ferrite content and becomes near the pure ferrite sample for $x = 80\%$ composite sample. The activation energy in ferromagnetic region is ranged from (0.2 to 0.23 eV) at different ferrite content as given in Table 6 which indicates the effect of ferroelectric phase of activation energy all samples. The

Table 5 Resistivity (ρ) and dielectric constant (ε) of composite samples

x (%)	ρ_{ac} (300 K) (Ω.cm)	ε at T_c			T_c (K)		
		10kHz	50 kHz	100 kHz	10 kHz	50 kHz	100 kHz
20	24	3.10	2.94	2.98	377	372	368
40	34	9.78	9.30	9.16	482	450	473
60	13	11.95	11.23	11.79	479	452	475
80	15	15.09	13.40	14.21	470	457	477

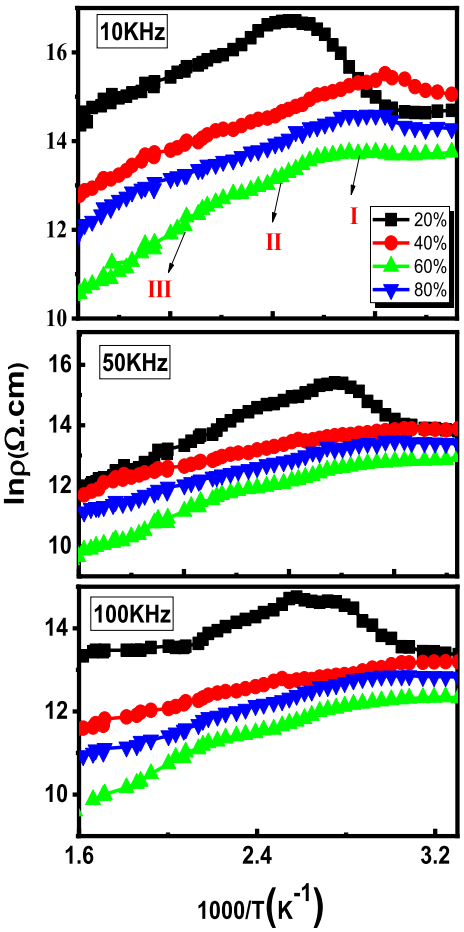

Fig. 6 The variation of ln ρ vs. 1000/T (K^{-1}) at different frequencies of composite samples

behavior of activation energy is similar to electrical resistivity, this mean that the high resistivity sample must have high activation energy. The conduction mechanism in the first region (ferroelectric state) can be explained by the fact that the barium acts as the donor so the increase in electric resistivity on the first region is caused by the increase in the distance between ($Ti^{+4} \leftrightarrow Ti^{+3}$) which decreases the conductivity and increases the resistivity [28]. The contribution of the *AC* part beside the *DC* conductivity for the

Table 6 Transition temperature and activation energy of ME composite at frequency 10kHz

x (%)	T_c (K) (ferro)	T_c (K) (ferrite)	T_c (K) (point conversion)	Activation energy for ferromagnetic region
20	386	507	413	0.20789
40	333	508	392	0.21538
60	343	512	389	0.26563
80	338	515	386	0.22773

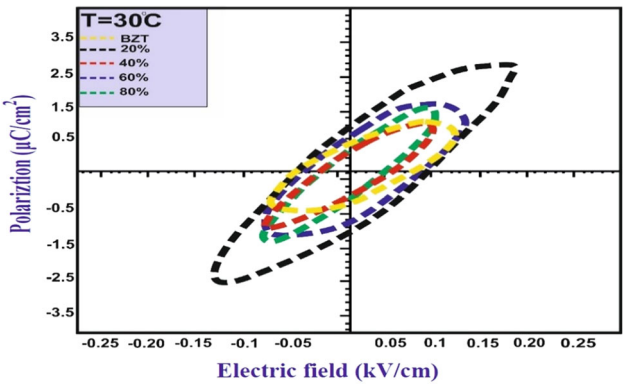

Fig. 7 The ferroelectric hysteresis loops of composite samples for different ferrite content (x%)

total conductivity of the composite sample. Can be expressed according the equation [29, 30]:

$$\sigma_T = \sigma_{DC} + \sigma_{AC} \quad (3)$$

where the σ_{DC} is the DC conductivity which is frequency independent and σ_{AC} is the AC conductivity which depends on both temperature and frequency [1]. The AC conductivity consist of two part according to the following equation:

$$\sigma_{Ac} = \sigma_1(T) + \sigma_2(\omega, T) \quad (4)$$

This means that the $\sigma_1(T)$ is temperature dependent and obeys the hopping conduction mechanism and is independent on frequency follows the Arrhenius equation

Table 7 Polarization values of the published works and our present data

Composite	Method	P (μC/cm^2)	Refs.
(1 − x) BST + (x) NCZMF	High-energy ball milling technique	2.56	[36]
Pb0.90Ba0.10(Zr0.53Ti0.47)O3 + 2% Nb2O5	Solid state reaction technique	2.80	[40]
Pb0.98La0.02(Zr0.90Ti0.10)0.995O3 + Ni0.64Zn0.36Fe2O4	High-energy ball milling technique	2.5	[41]
(1 − x) (BZT) + (CZLF)	High-energy ball milling technique	2.93	Present work

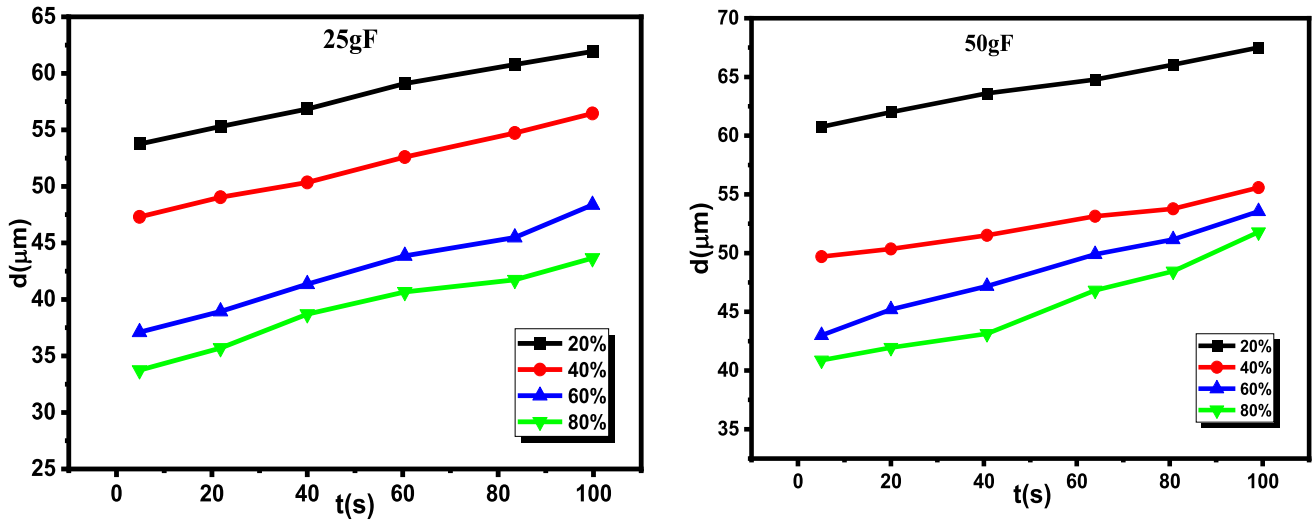

Fig. 8 The creep distance is plotted versus the indentation time of different loads 50gF and 25gF CZLF/BZT composite

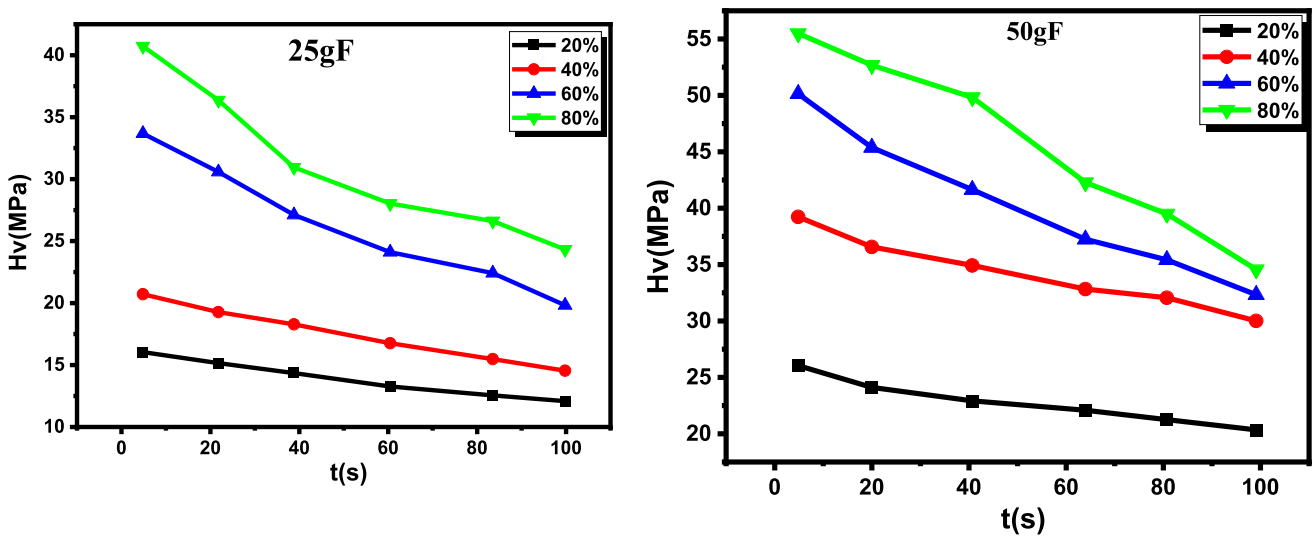

Fig. 9 Vickers hardness (H_V) behavior of CZLF/BZT composite

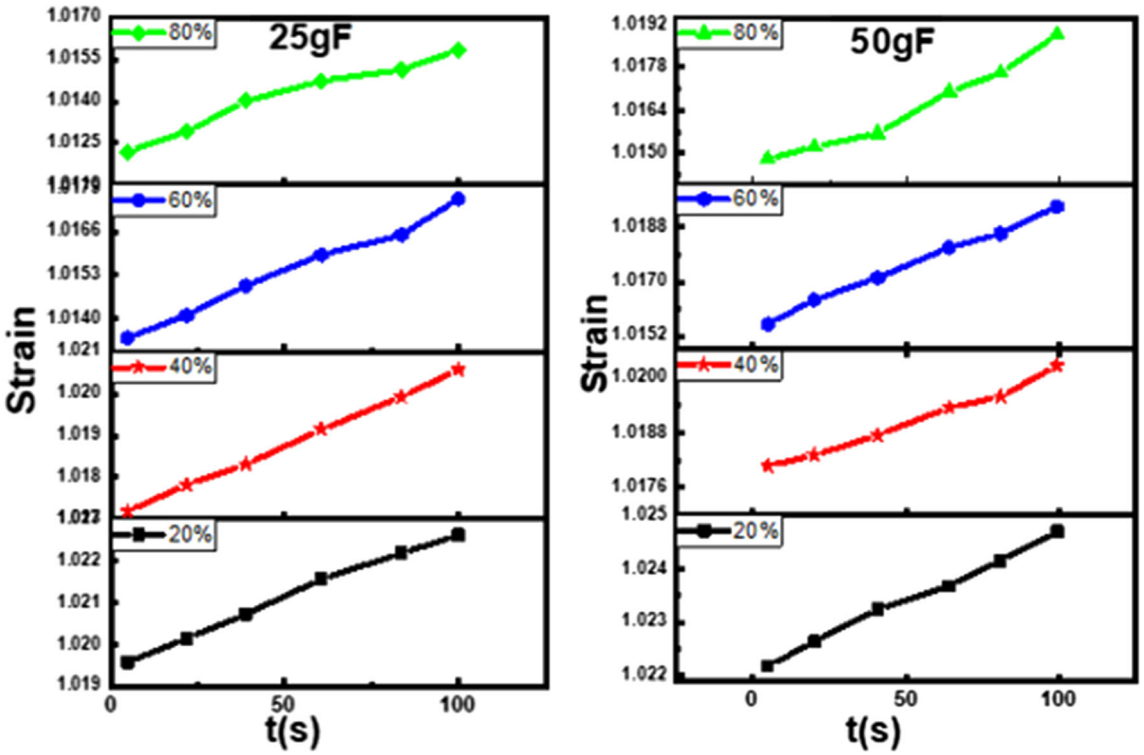

Fig. 10 Strain behavior of CZLF/BZT composite

Table 8 The theoretical and experimental values of hardness and stress component of CZLF/BZT composites

x (%)	Load	Hv (MPa) Theoretical	*n* (log Hv vs. log t)	*n* (log d* vs. log Hv)	Grain size (μm)	Crystalline size
20	25	14	1.75	0.15	0.172	32
	50	23	2.08	0.12		
40	25	18	1.90	0.15	0.208	30
	50	34	2.36	0.10		
60	25	26	2.15	0.15	0.303	28
	50	40	2.45	0.13		
80	25	31	2.27	0.13	0.365	24
	50	46	2.53	0.12		

$$\rho = \rho_0 e^{\frac{\Delta E}{KT}} \tag{5}$$

3.4. Ferroelectric hysteresis loops of composite samples

Figure 7 shows the dielectric hysteresis loop (*P*–*E*) plot for the composite sample $(1 - x)$ $BaZr_{0.5}Ti_{0.5}O_3$ (BZT) + $xCo_{0.65}Zn_{0.35}La_{0.02}Fe_{1.98}O_4$ (CZLF), where x = 20%, 40%, 60% and 80% were displayed using Sawer-Tawer modified circuit [31]. It is noticed from the figure that the area of hysteresis loop decreases by increasing ferrite content. Which indicates that the dielectric loss decreases by increasing ferrite content [32].

The saturation polarization (P_s) decreases by increasing ferrite content because the ferrite nano particle obstructs the rotation of the dielectric dipoles in the field direction leading to the decrease in dipolar polarization [33, 34].The unsaturated (*P*–*E*) loop to leakage current after the addition of ferrite this is similar to previous result as shown Table 7 [35, 36]. The Curie temperature (T_c) increases by increasing ferrite content which means that the ferrite resistance that from the transformation ferroelectric phase to paraelectric phase [37–39].

3.5. Mechanical properties

The hardness of the material represents the resistance to the lattice distortion and permanent damage of permanence [42]. The expression Hardness include information about the yield strength, molecular binding and some other elastic constant, which is related to the micro hardness

study of the crystal and need to subject the material to pressure stress in a specific area. Figure 8 shows the creep distance behavior of the composite sample $(1-x)$ $BaZr_{0.5}Ti_{0.5}O_3$ (BZT) + x $Co_{0.65}Zn_{0.35}La_{0.02}Fe_{1.98}O_4$ (CZLF), where x = 20%, 40%, 60% and 80% at different ferrite content and to applied loads 50 gF,25 gF versus creep time (t).

From this figure it is noticed that the creep distance increases by increasing time and decreases by increasing ferrite content. It was also seen that the creep distance increases by increasing the applied load.

The Vickers hardness is related to the plastic deformation of the material and can be theoretically calculated from the following formula

$$Hv = 1.854\frac{F}{d^2} \tag{6}$$

where d is the mean diagonal value of the indentation in mm and F is the load in Kg [43]. Figure 9 shows the variation of Vickers hardness (H_v) is plotted against the creep time for both applied load 25 gF, 50 gF. It was noticed clearly that the Vickers hardness decreases by increasing time and increases by increasing the ferrite content which is may be due to the good desperation of high hardness ferrite in the composite material [44]. At low time the composite sample has high creep resistance and high H_v, where it decreases sharply at high time. The factor of the H_v decrease from (40 to 25 Mpa) for the sample x = 80% is higher than the other samples which is explained by the brittle nature of ferrite.

Figure 10 shows the variation of strain and indentation time applied for all sample at different applied load 25 gF, 50 gF. *It* is noticed from the figure the indentation strain increases by increasing the time and decreases by increasing ferrite content. The indentation strain decreases by increasing ferrite content, whereas the creep resistance H_v increases which has attributed to the small crystalline size in the composite. As the grain size increases the material becomes more rigid and hardness.

Theoretical hardness was calculated and listed in Table 8. The theoretical and experimental values are very close.

4. Conclusions

In present work, $(1-x)$ $BaZr_{0.5}Ti_{0.5}O_3$ + $xCo_{0.65}Zn_{0.35}La_{0.02}$ $Fe_{1.98}O_4$ (CZLF-BZT) (where x = 20%, 40%, 60% and 80%) was successfully prepared by high-energy ball milling method. Structural, impedance and dielectric properties of the synthesized composites were investigated and discussed in detail. The x-ray diffraction technique shows that all the samples possessed a double-phase polycrystalline sample with a tetragonal–rhombohedral structure. Impedance and dielectric behavior were investigated in a wide range of temperatures (room temperature—573 K) and frequency (100 Hz $\leq$ f $\leq$ 1 MHz). A broad dielectric constant peak was observed around the phase transition temperature. A broad dielectric constant peak was observed around the phase transition temperature. The Nyquist plots revealed the existence of grain and grain boundaries in the overall impedance. The value of activation energy in general decreases by increasing ferroelectric content which indicates the effect of ferroelectric phase on the value of activation energy. The ferroelectric hysteresis loop becomes narrow as the temperature increases, which indicates the damage of the ferroelectric order of the BZT due to the addition of ferrite and is closed near Curie temperature for all composite samples. The length of creep increases by increasing the load and the time for each load. The hardness decreases by increasing time in the interval from 5 to 100 s. The sample below 25 gF load has a high creep resistance (high H_v). From the value of the stress component, the mechanism of creeping in CZLF/BZT composite sample is due to the grain boundary sliding. The indentation strain increases by increasing the load time.

Funding Open access funding provided by The Science, Technology & Innovation Funding Authority (STDF) in cooperation with The Egyptian Knowledge Bank (EKB).

References

[1] S Shankar, O P Thakur and M Jayasimhadri *J. Electron. Mater.* **49** 472 (2020)
[2] E Sumalatha, N Hari kumar, A Edukondalu and D Ravinder *Inorg. Chem. Commun.* **146** 110200 (2022)
[3] H X Zhang, P F Wang, et al. Yao *Rare Met.* (2023)
[4] Z Wu, B Lin, J Fan, J Zhao, Q Zhang and L Li *IEEE Trans. Dielectr. Electr. Insulation* **29** 1651 (2022)
[5] K M Sangwan, N Ahlawat, R S Kundu, S Rani and S Rani AIP Conference Proceedings **2115** (2019)

[6] R Dewi, Y Hamzah, Zulkarnain, Krisman, A S Rini and T S L H Shahab Journal of Physics: Conference Series **1655** p 1 (2020)
[7] S.Shankar, O P Thakur and M Jayasimhadri *Mater. Chem. Phys.* **234** 110 (2019)
[8] X Zhang, Y Tang, F Zhang and C S Lee *Adv. Energy Mater.* **6** 1 (2016)
[9] A S Gaikwad, R H Kadam, S E Shirsath, S R Wadgane, J Shah, R K Kotnala and A B Kadam *J. Alloys Compd.* **773** 564 (2019)
[10] S R Wadgane, S T Alone, A Karim, G Vats, S E Shirsath and R H Kadam *J. Magn. Magn. Mater.* **471** 388 (2019)
[11] S S Choudhari, S R Wadgane, B P Gaikwad, S S Satpute, K M Batoo, O M Aldossary, S E Shirsath and R H Kadam *Ceram. Int.* **47** 6496 (2021)
[12] J Zhao, J Gao, W Li, Y Qian, X Shen, X Wang, X Shen, Z Hu, C Dong, Q Huang, L Cao, Z Li, J Zhang, C Ren, L Duan, Q Liu, R Yu, Y Ren, S C Weng et al *Nat. Commun.* **12** 1 (2021).
[13] S S Choudhari, S B Shelke, K M Batoo, S F Adil, A B Kadam, A Imran, M Hadi, E H Raslan, S E Shirsath and R H Kadam *J. Mater. Sci. Mater. Electron.* **32** 10308 (2021)
[14] S T Yang, X Y Li, T L Yu, J Wang, H Fang, F Nie, B He, L Zhao, W M Lü, S S Yan, A Nogaret, G Liu and L M Zheng *Adv. Funct. Mater.* **32** 1 (2022)
[15] A M Henaish, M Mostafa, I Weinstein, O Hemeda and B Salem *Magnetism* **1** 22 (2021)
[16] A M Altarawneh, E A Arrasheed, A Ajlouni, R Ghazy, O M Hemeda, A M A Henaish and M Mostafa *Ceram. Int.* 1 (2023)
[17] G Akgul and F A Akgul *Colloids Interface Sci. Commun.* **48** 100611 (2022)
[18] M M Salem, M A Darwish, et al. *Rsc Adv.* **14** 3335 (2024)
[19] K P S Parmar, J H Kim, A Bist, P Dua, P K Tiwari, A Phuruangrat, and J S Lee *ACS Omega* **7** 31607 (2022)
[20] F R Mariosi, J Venturini, A da Cas Viegas and C P Bergmann *Ceram. Int.* **46** 2772 (2020).
[21] R Rani, K M Batoo, P Sharma, G Anand, G Kumar, S Bhardwaj and M Singh *Ceram. Int.* **47** 30902 (2021)
[22] S S Choudhari, S B Shelke, K M Batoo, S F Adil and R H Kadam *J. Mater. Sci. Mater. Electron.* **32** 10308 (2021)
[23] S A Mazen, A S Nawara and N I Abu-Elsaad *Ceram. Int.* **47** 9856 (2021).
[24] S Shankar, M Kumar, P Brijmohan, S Kumar, O P Thakur and A K Ghosh *J. Mater. Sci. Mater. Electron.* **27** 13259 (2016)
[25] M Rawat and K L Yadav *IEEE Trans. Dielectr. Electr. Insulation* **22** 1462 (2015).
[26] K Mujasam, S Kumar and C Gyu n.d.
[27] S A Raza, S U Awan, S Hussain, S A Shah, A M Iqbal and S Khurshid Hasanain *J. Appl. Phys.* **128** 124101 (2020)
[28] S Manzoor, S Husain, A Somvanshi and M Fatema *J. Mater. Sci. Mater. Electron.* **31** 7811 (2020)
[29] A S Dzunuzovic, M M V Petrovic, J D Bobic, N I Ilic and B D Stojanovic *J. Electroceram.* **46** 57 (2021)
[30] J Massoudi, O Messaoudi, S Gharb, T Mnasri, E Dhahri, K Khirouni, EK Hlil and L Alfhaid *Phys. Chem. Chem. Phys.* 6 (2022)
[31] G Ferrero, K Astafiev, E Ringgaard, L S de Oliveira, B R Sudireddy, A B Haugen, K Žiberna, B Malič and T Rojac *J. Eur. Ceram. Soc.* **43** 350 (2023)
[32] X Zhang, P Jiao, H Cheng, K Xiong, J Yang, L Chen, J Zhou, Z Zhu, J Zhang, J Luo, J Wang, Y Yang, S T Zhang, D Wu and J M Liu *Adv. Electron. Mater.* **8** 1 (2022)
[33] D Bochenek, P Niemiec and A Chrobak *Materials* **14** 2488 (2021)
[34] M Thakur and S K Sharma AIP Conference Proceedings **2451** (2022)
[35] O M Hemeda, A Tawfik, D E El Refaey, A H El-Sayed and S Mohamed *Open J. Appl. Sci.* **7** 559 (2017)
[36] B I Salem, O M Hemeda, M Mostafa and A M A Henaish *J. Mater. Sci. Mater. Electron.* **31** 18673 (2020)
[37] N Krishna and K G Padmasine *Mater. Sci. Semicond. Process.* **154** 107181 (2023).
[38] S Priya Balmuchu, S R N K Mangalampalli and P Dobbidi *Mater. Sci. Eng. B Solid-State Mater. Adv. Technol.* **282** 115791 (2022)
[39] H Gouadria, M Smari, T Mnasri, J Necib, J López Sánchez, P Marín, A P Jamale and R Ben Younes *Inorg. Chem. Commun.* **147** 110241(2023)
[40] D Bochenek, A Chrobak and G Dercz *Materials* **15** 8461 (2022)
[41] D Bochenek, P Niemiec, J Korzekwa, B Durtka and Z Stokłosa *Symmetry* **10** 59 (2018)
[42] R M Shalaby *J. Alloys Compd.* **505** 113 (2010)
[43] Obuda University *Mechanical properties laboratory practice guide* p 1 (2015)
[44] A T Olanipekun, M Nthabiseng, O O Ayodele, M R Mphahlele, B M Mampuya and P A Olubambi *Data Brief* **27** 104551 (2019)